

Three-dimensional flow structures and evolution of the leading-edge vortices on a flapping wing

Yuan Lu* and Gong Xin Shen†

Full Flow Field Observation and Measurement, Institute of Fluid Mechanics, Beijing University of Aeronautics and Astronautics, Beijing 100083, People's Republic of China

*Present address: Department of Mechanical Engineering, Johns Hopkins University, Baltimore, MD 21218, USA

†Author for correspondence (e-mail: gx_shen55@yahoo.com.cn)

Accepted 16 February 2008

SUMMARY

Following the identification and confirmation of the substructures of the leading-edge vortex (LEV) system on flapping wings, it is apparent that the actual LEV structures could be more complex than had been estimated in previous investigations. In this experimental study, we reveal for the first time the detailed three-dimensional (3-D) flow structures and evolution of the LEVs on a flapping wing in the hovering condition at high Reynolds number ($Re=1624$). This was accomplished by utilizing an electromechanical model dragonfly wing flapping in a water tank (mid-stroke angle of attack= 60°) and applying phase-lock based multi-slice digital stereoscopic particle image velocimetry (DSPIV) to measure the target flow fields at three typical stroke phases: at $0.125T$ (T =stroke period), when the wing was accelerating; at $0.25T$, when the wing had maximum speed; and at $0.375T$, when the wing was decelerating. The result shows that the LEV system is a collection of four vortical elements: one primary vortex and three minor vortices, instead of a single conical or tube-like vortex as reported or hypothesized in previous studies. These vortical elements are highly time-dependent in structure and show distinct 'stay properties' at different spanwise sections. The spanwise flows are also time-dependent, not only in the velocity magnitude but also in direction.

Key words: flapping wing, hovering, flow structure, leading-edge vortex (LEV), vortex shedding, electromechanical model, digital stereoscopic particle image velocimetry (DSPIV).

INTRODUCTION

In the domain of flapping flight, the attached leading-edge vortex (LEV) has been identified as a crucial high-lift source and subjected to considerable investigations (Ellington et al., 1996; Van Den Berg and Ellington, 1997; Liu et al., 1998; Dickinson et al., 1999; Birch and Dickinson, 2001; Sun and Tang, 2002; Birch et al., 2004; Wu and Sun, 2004; Bomphrey et al., 2005). The substructure of this vortical system was reported by Srygley and Thomas (Srygley and Thomas, 2002), and recently rediscovered (Lu et al., 2007) and confirmed (Lu et al., 2006). Furthermore, the LEV shedding was observed at the outer wing (Lu et al., 2006), which had not been reported before. These new discoveries strongly suggested that the complexity of the LEV system had been underestimated in the earlier investigations. As a result of the 3-D and unsteady nature of the flapping wing LEV system, not only the 3-D flow measurement technique but also systematic study of the different phases within a stroke period are required to reveal its actual flow structure and evolution. In fact, this knowledge is of fundamental significance as it serves as a basis for the more intricate case of dragonfly flight with forewing–hindwing interactions.

As far as we know, there have been only a limited number of studies addressing the 3-D flow structures and evolution of the flapping wing LEVs. Liu et al. conducted a computational study of hawkmoth hovering at high Reynold's number ($Re\sim 3000$) and presented the 3-D LEV structures in evolutionary sequence (Liu et al., 1998), but the vortical structures were represented *via* the 3-D streamlines, which could not educe the topological structures of the vortices and would be problematic when interpreting the

unsteady flow field (Hama, 1962). Recently, digital stereoscopic PIV (DSPIV), a 2D3C (two-dimensional, three-velocity components) flow imaging technique involving two cameras positioned at the stereoscopic configuration (Arroyo and Greated, 1991), was implemented for measurement of the full flow field around a flapping model fruitfly wing ($Re\sim 100$) at various time steps (Poelma et al., 2006). Based on the acquired 3-D data, the velocity gradient tensor ($\nabla \mathbf{u}$) based vortex identification criterion was applied, which effectively visualized accurately those vortical structures that could not be obtained from qualitative visualizations (smokes, bubbles or dyes) and the common quantitative plots (3-D streamlines or iso-vorticity surfaces). Nevertheless, the focus of that work was the general flow field, rather than detailed structure of the LEV system. More importantly, the LEV system at such low Re values would be structurally simpler than that in the high Re situation (Birch et al., 2004; Lu et al., 2006). Since the typical Re of dragonflies is relatively high, of the order of 1000 (Dudley, 2000), and larger flapping wing vehicles could more likely be realized, knowledge of the LEV system at high Re is more desirable.

Here, as an extension of our previous work (Lu et al., 2006), we reveal for the first time detailed 3-D structures and evolution of the LEVs on a flapping wing. Based upon an electromechanical model dragonfly wing flapping in a water tank (at $Re=1624$), the DSPIV technique was implemented. Thanks to the periodic nature of the flows, we were able to take measurements at different spanwise locations at separated times for a given stroke phase by employing the phase-lock technique. These 2D3C velocity vectors

were then assembled along the spanwise direction and formed a 3D3C velocity field. The evolution of the LEV system was examined by applying the above procedure to three typical stroke phases: (1) at $0.125T$ (T =stroke period), when the wing was accelerating, (2) at $0.25T$, when the wing was moving at maximum speed, and (3) at $0.375T$, when the wing was decelerating. Using these 3D3C velocity data, four vortex identification criteria [$|\omega|$ -criterion, Δ -criterion (Chong et al., 1990), Q -criterion (Hunt et al., 1988) and λ_2 -criterion (Jeong and Hussain, 1995)] were tested to find out the most suitable criterion for reconstructing accurate vortical structures.

MATERIALS AND METHODS

Model wing and kinematic simulation

The model wing used here was a simplified version of a dragonfly wing [aspect ratio $AR=5.8$, $AR=R/c$, where $R=150$ mm is the model wing length, measured from the translational axis (oy) to the wing-tip; c is the mean wing chord length; see Fig. 1A, left for the wing planform]. The wing planform used here was not only as a simplification, but also to eliminate the geometric effects to the LEV system, which could cause potential interference. For

example, corrugation of the wing surface could generate small-scale vortices (Luo and Sun, 2005), which might coexist together with the LEV sub-structures, rendering it difficult to differentiate between them. Other geometric factors such as the curvature of the leading edge as well as the camber might have certain effects on the LEV system, but there are few reports that systematically address this issue. Hence it would not be sensible to add such factors, whose effects are not well studied, to the current experimental system. Mechanical constraints meant that the model wing was mounted on the tip of the rotational shaft, and the wing base was 46 mm away from the translational axis, rendering the effective wing length (r)=104 mm for the model wing (see Fig. 1A, left). The model wing was fabricated from a flat aluminium sheet (1 mm thick; c -based normalized thickness=3.8%). The wing surfaces were painted black to inhibit laser reflection in the DSPIV experiment.

The flapping kinematics included two degrees of freedom (d.f.): translation and rotation. As sketched in Fig. 1B, translation is the azimuthal rotation of the wing about the translational axis oy , and rotation is the supinating/pronating rotation about the axis oz (located at $1/4$ wing chord from the leading-edge, denoted in Fig. 1A as a thick black line). D and U in Fig. 1A are two translational extremes, and they define the horizontal stroke plane and the stroke amplitude Φ . The instantaneous translational angle $\varphi(t)$ varied as the cosine function (Ellington, 1984):

$$\varphi(t) = 0.5\Phi[1 - \cos(2\pi t/T)]. \quad (1)$$

The instantaneous rotational angle $\rho(t)$ [$\rho(t)=90^\circ-\alpha(t)^\circ$, where $\alpha(t)$ =instantaneous angle of attack; ρ_M =the maximal rotational angle, relating with the mid-stroke angle of attack $\alpha_{mid}=90^\circ-\rho_M^\circ$] varied as a simple harmonic function when the wing was undergoing rotation, but remained constant when the wing was purely translating. The duration of rotation ΔT_r was fixed at $0.2T$, thus the rotational function in one period was:

$$\rho(t) = \begin{cases} \rho_M \sin[\pi(t)/\Delta T_r] & 0 \leq t < 0.1T \\ \rho_M & 0.1T \leq t < 0.4T \\ \rho_M \cos[\pi(t-0.4T)/\Delta T_r] & 0.4T \leq t < 0.6T \\ -\rho_M & 0.6T \leq t < 0.9T \\ -\rho_M \cos[\pi(t-0.9T)/\Delta T_r] & 0.9T \leq t < T \end{cases} \quad (2)$$

The kinematic curves are plotted in Fig. 1B. Here, Φ was set to 60° , the same as for the dragonfly hovering (Norberg, 1975). Dragonflies use incline stroke plane in hovering flight (Norberg, 1975), necessitating an asymmetric kinematic pattern of down- and upstrokes for weight support and thrust cancellation (Wang, 2000a; Wang, 2004). Thus the angle of attack in downstroke ($\alpha_{mid}=60^\circ$) is larger than that in upstroke ($\alpha_{mid}=30^\circ$). However, according to our observations, the LEVs produced at the same angle of attack but in symmetric and asymmetric strokes show no detectable difference in structure (Lu et al., 2006; Lu et al., 2007). Because the sub-LEV structures were observed to be more conspicuous at $\alpha_{mid}=60^\circ$ than those at $\alpha_{mid}=30^\circ$ (Lu et al., 2006), we set $\alpha_{mid}=60^\circ$ for the model wing ($\rho_M=30^\circ$). The stroke frequency n ($=1/T$) was set to 0.2 Hz so that $Re=1624$ [$Re=U_{tip}c/\nu$, where U_{tip} =mean wing-tip speed; ν =kinematic viscosity (Ellington, 1984); here, since $U_{tip}=2\Phi nR$, $Re=2\Phi nRc/\nu$], within the range of dragonfly hovering (Dudley, 2000).

The flapping motions were mimicked *via* a self-designed electromechanical system introduced previously (Lu et al., 2006). In this study, because the down- and upstroke motions were symmetric, only the phases in the downstroke were measured.

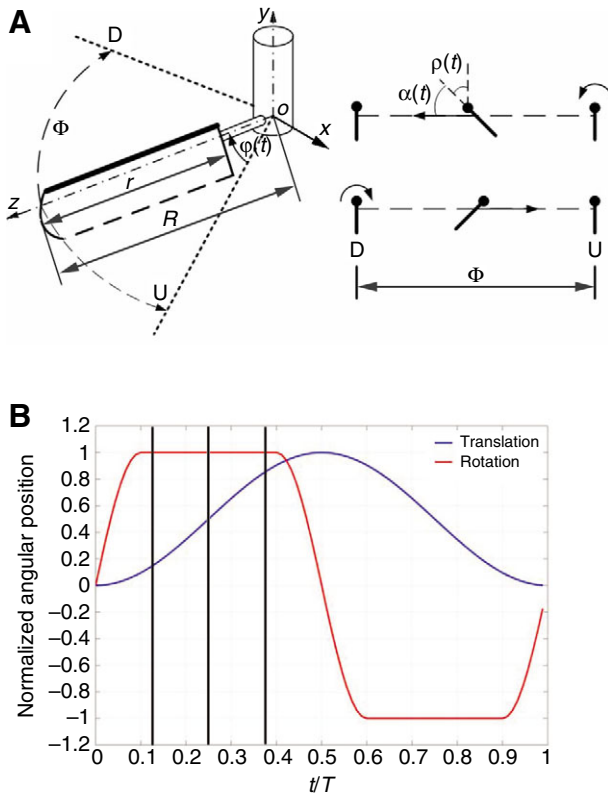


Fig. 1. The model wing and the flapping motions. (A) Left: spatial configuration of the flapping motion of the model wing. $oxyz$, the wing-fixed frame (y -axis vertical to the ground); D and U, the translational extreme positions; R , model wing length; r , effective model wing length; Φ , stroke amplitude; $\varphi(t)$, instantaneous translational angle. The thick black line denotes the leading edge. Right: the motion of a section of the wing. $\alpha(t)$, instantaneous angle of attack; $\rho(t)$, instantaneous rotational angle [$\rho(t)=90^\circ-\alpha(t)^\circ$]. The black thick line denotes wing section and the solid-dot the leading edge. (B) The kinematic curves in one period. The translational and rotational angular positions are normalized using Φ and ρ_M (the maximal rotational angle), respectively. The black lines at $t/T=0.125$, 0.25 and 0.375 denote the DSPIV measurement phases.

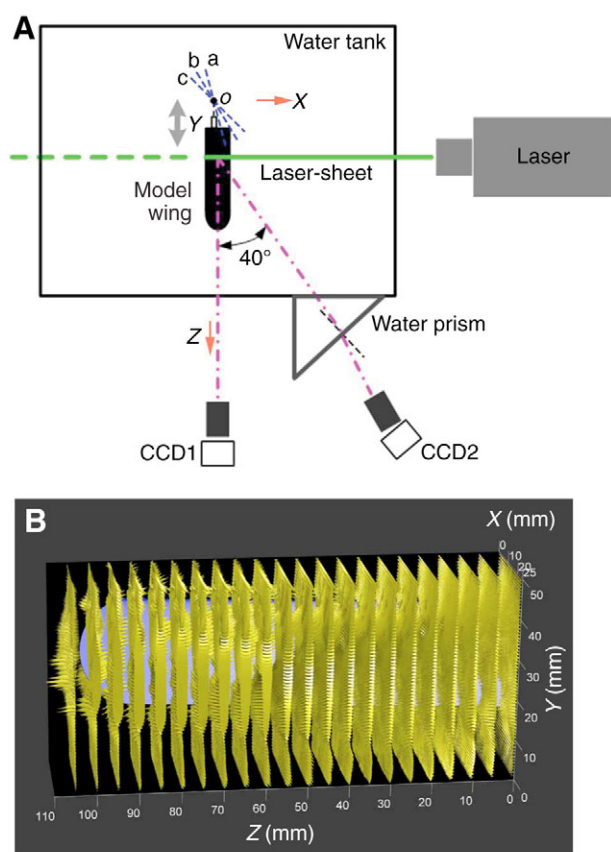


Fig. 2. DSPIV setup. (A) The DSPIV experimental arrangement (top view). CCD1 and CCD2 are the CCD cameras. The broken-line section of the laser-sheet represents the shadow behind the opaque model wing. The blue broken lines a, b and c around the origin *o* are the initial positions of 0.125*T*, 0.25*T* and 0.375*T*, respectively. At the instant of measurement, the wing-fixed frame *oxyz* coincided with the inertial frame *oXYZ*. The thick gray double-headed arrow denotes the positioning translation of the model system. (B) The typical raw 3D3C velocity field (at 0.25*T*) before spanwise interpolation. The blue region is the model wing.

DSPIV measurement and 3-D flow field reconstruction

A small measurement window (horizontal \times vertical=25 mm \times 50 mm), making full use of the CCD resolution while properly containing all LEV elements, was quantified *via* DSPIV in a water tank (length \times width \times depth=600 mm \times 400 mm \times 400 mm). The electromechanical system was mounted on a positioning translation system (the translating direction was perpendicular to the laser-sheet) on the top of the tank, and thus it was possible to measure at different spanwise locations without displacing the DSPIV apparatus. The initial positions of the wing (denoted a, b, c in Fig. 2A) were well adjusted, ensuring the spanwise direction of the wing to be perpendicular to the laser-sheet at given stroke phase (0.125*T*, 0.25*T* and 0.375*T*).

A 3 mm thick laser-sheet was created by a dual-pulse Nd-Yag laser system (maximum of 200 mJ pulse⁻¹, LABest, Beijing, China). Two CCD cameras (1080 pixels \times 1920 pixels, Red Lake, San Diego, CA, USA) with the close-up lenses (Micro Nikkor 105 mm f/2.8, Nikon, Tokyo, Japan) on Scheimpflug mounts were positioned as an asymmetric angular-displacement configuration (Coudert et al., 2000). The left camera (CCD1) was perpendicular to the laser-sheet, as in the classical 2-D DPIV arrangement, while the right counterpart (CCD2) viewed obliquely through a water-filled prism

with an effective angle of roughly 40° with respect to the laser-sheet normal (see Fig. 2A). The water prism was utilized so that the oblique-viewing camera had a nearly orthogonal orientation with respect to the liquid–air interface. This method effectively reduced radial distortions owing to the large off-axis angle (Prasad and Jensen, 1995). Coudert et al. (Coudert et al., 2000) pointed out that the asymmetry of the stereo setup is, in fact, propitious to the precision of a DSPIV system [measured by the error ratio: the ratio of the out-of-plane root mean square (r.m.s.) error to the in-plane r.m.s. error (Lawson and Wu, 1997b)]. The present asymmetric arrangement is expected to achieve an error ratio <2.5 (Coudert et al., 2000). Following the proposal of Lawson and Wu (Lawson and Wu, 1997a), the aperture of *f*/16 (*f*=focal length) was set for both lenses to have a large depth of focus.

Calibration was carried out based on a 25 mm \times 40 mm (horizontal \times vertical) rectangle region (the calibration target), which was marked with a grid of 21 \times 37 filled circles and printed on a plate mounted on the positioning translation rail. The calibration target was recorded by both cameras at five 0.5 mm-spaced locations across the laser-sheet width. Because the recorded images (especially those viewed by the oblique camera CCD2) were distorted due to the deviation of the lens axis from the calibration plate normal, they were at first dewarped to have an orthogonal coordinate (Willert, 1997). Then the calibration coefficients, which would back-project the left and right pixel-based 2D2C displacements onto the 2D3C physical displacements, were calculated for the dewarped images using the least-squares polynomial approach (Soloff et al., 1997).

After calibration, the water was seeded with hollow glass beads (1–5 μ m diameter), and the measurements of the target flow fields performed. Due to the periodic nature of the flows generated in flapping motions, we could measure different spanwise locations at separated times for each stroke phase. This was done based on the phase-lock technique, which relies on two digital delay/pulse generators (DG 535, Stanford Research System Co., Sunnyvale, CA, USA) to ensure synchronization of the laser pair triggering, the image pair recording and the wing motion. A laser-pulse separation of 4 ms was set for the case of 0.125*T*, and 2 ms for both cases of 0.25*T* and 0.375*T*. For each stroke phase, 23 spanwise locations (5 mm-spacings), ranging from the wing-base to the region beyond the wing-tip, were measured. For each spanwise location, 30 periods were sampled, but the first five periods were discarded to avoid the ‘start-up effect’.

Although the model wing was painted black, the laser reflections were still strong in the particle images, which would lead to spurious vectors in the following cross-correlation. Here, they were removed by subtracting an average background image, which was produced by averaging all frames in the same sequence so that the particle grayscale were adequately lower than that of the reflections (Fore et al., 2005). The reflection-free particle images were then preconditioned using a simple approach (Shavit et al., 2006), which could effectively inhibit the spurious vectors in the cross-correlation. All preconditioning and post-processing were operated in Matlab. For convenience of manipulation, we used MatPIV v.1.6.1, an open-source code for Matlab (Sveen, 2004) to cross-correlate the image sequences. Multiple-pass with the final interrogation window of 16 pixels \times 16 pixels was used, generating excellent vector maps. The vector maps of the same sequence were averaged to generate the mean vector field. Since misalignment between the laser-sheet and the calibration target was inevitable (Willert, 1997; Coudert and Schon, 2001), a correction based upon the ‘disparity map’ (Willert, 1997; Coudert and Schon, 2001) was performed. Finally, the left

and right 2D2C vectors were back-projected to the 2D3C vectors using the calculated calibration coefficients.

For each stroke phase, the 2D3C arrays were assembled along the spanwise direction (Z) and formed an $111 \times 55 \times 23$ matrix. The raw 3D3C vector field is shown in Fig. 2B. It was then interpolated along the Z -direction to make all dimensions have equal spacing between the grid points. The final size of the 3-D matrices was $111 \times 55 \times 245$. Subsequently, the vorticity field ($\boldsymbol{\omega}$), velocity gradient tensor ($\nabla \mathbf{u}$) and the relevant quantities were calculated.

Vortex identification

A proper vortex identification criterion is critical in the current study. We tested four well known criteria, which are based on the velocity gradient tensor $\nabla \mathbf{u} = \partial u_i / \partial x_j$ (where i and j are the indices; $i, j = 1, 2, 3$), with the acquired 3D3C velocity field.

(1) $|\boldsymbol{\omega}|$ -criterion. $|\boldsymbol{\omega}|$ is the norm of the vorticity vector ($\boldsymbol{\omega} = \nabla \times \mathbf{u}$). This criterion identifies a flow region as a vortex when $|\boldsymbol{\omega}|$ reaches a specified threshold.

(2) Δ -criterion. Δ is the discriminant of $\nabla \mathbf{u}$'s characteristic equation. It defines a region as a vortex if every point in this region has $\Delta > 0$ (Chong et al., 1990). Δ governs the instantaneous local stream patterns in a frame that is relatively at rest with respect to the fluid particle. When $\Delta > 0$, $\nabla \mathbf{u}$ has complex eigenvalues, and the instantaneous streamlines are locally closed or spiral (Chong et al., 1990).

(3) Q -criterion. Q is the second invariant of $\nabla \mathbf{u}$. It defines a region as a vortex if every point in this region has $Q > 0$ (Hunt et al., 1988). In incompressible flow ($\nabla \cdot \mathbf{u} = 0$), $Q = 0.5(\|\boldsymbol{\Omega}\|_E^2 - \|\mathbf{S}\|_E^2)$, where $\boldsymbol{\Omega} = 0.5(\nabla \mathbf{u} - \nabla \mathbf{u}^T)$ (T denotes the transpose) and $\mathbf{S} = 0.5(\nabla \mathbf{u} + \nabla \mathbf{u}^T)$ are the asymmetric and symmetric components of $\nabla \mathbf{u}$, respectively; $\|\mathbf{A}\|_E = \sqrt{\text{tr}(\mathbf{A}\mathbf{A}^T)}$ is the Euclid norm of a given tensor \mathbf{A} . Q indicates

the local competition between the rotation rate and deformation (or strain) rate, thus $Q > 0$ means that the local rotational effect dominates (Hunt et al., 1988).

(4) λ_2 -criterion. λ_2 is the intermediate eigenvalue of the symmetric tensor $\boldsymbol{\Omega}^2 + \mathbf{S}^2$, which relates the pressure P with the relation: $\boldsymbol{\Omega}^2 + \mathbf{S}^2 = -1/\rho[\nabla(\nabla P)]$ when discarding the effects of unsteadiness and viscosity (Jeong and Hussain, 1995). This criterion defines a region as a vortex if every point in this region has $\lambda_2 < 0$, since $\lambda_2 < 0$ implies that the plane perpendicular to the local vortex axis has the local pressure minimum (Jeong and Hussain, 1995).

Fig. 3 shows the visualizations obtained using these four criteria. Data obtained at $0.25T$ were used for testing because at this instant the vortical system had the most intricate structure. The values of $|\boldsymbol{\omega}|$, Δ and Q were normalized by their maxima (>0), while the value of λ_2 was normalized by the minimum (<0). The thresholds of the criteria were selected carefully so that the isosurfaces described the basic and close topological structures of the same vortices.

It can be seen that the $|\boldsymbol{\omega}|$ -criterion, although visualizing the general structures, had the disadvantage of also showing the shear-layers near the wing surface and between the vortices. The reconstruction of the Δ -criterion showed substantial noise, and the borders between the target vortices were obscured. Both of the other two criteria showed the interesting details more clearly, and illustrated nearly identical structures owing to their mathematical and physical similarities (Jeong and Hussain, 1995; Cucitore et al., 1999; Chakraborty et al., 2005). Since the Q -value offers more abundant information about the local flow field, e.g. $Q < 0$ means the local deformation-rate dominates, we chose it as the chief criterion in this study. Note that the isosurfaces deduced by these criteria are the vortex core structures, but not the vortex tubes as defined (Saffman, 1992).

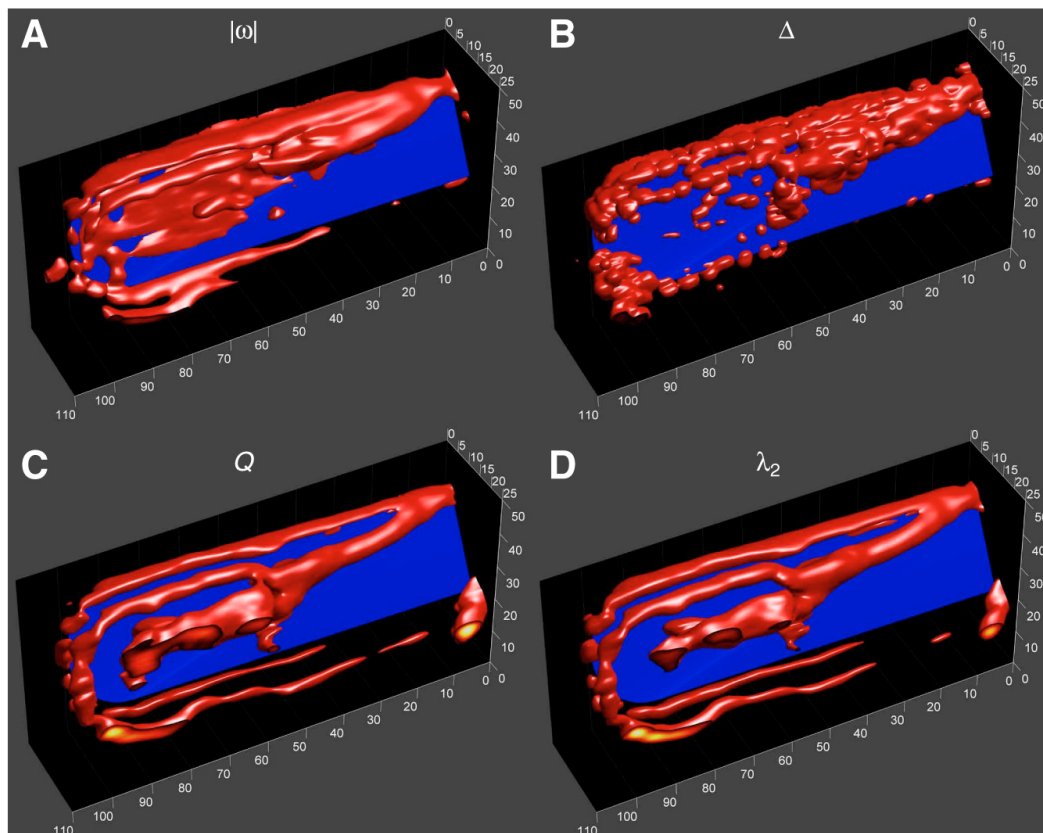


Fig. 3. The test of four vortex identification criteria. Data at $0.25T$, when the vortical system was most intricate, were tested. The dimensionless values of the iso-surfaces (the red regions) of $|\boldsymbol{\omega}|$, Δ , Q and λ_2 are 0.22, 0.00015, 0.09 and 0.04, respectively. The values of $|\boldsymbol{\omega}|$, Δ and Q are normalized by their maxima (>0), whereas the value of λ_2 is normalized by the minimum (<0). The blue plate is the model wing.

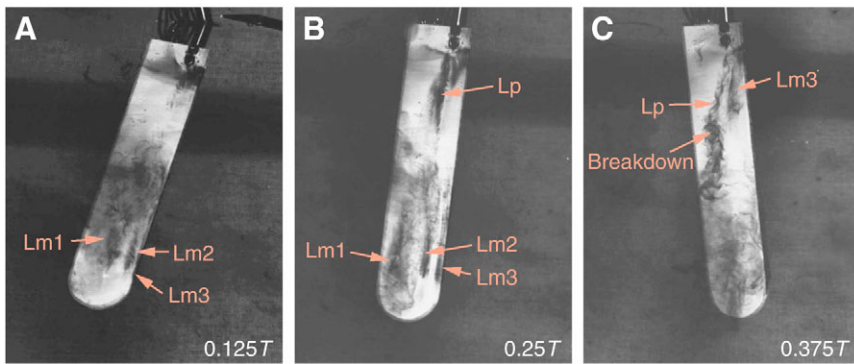


Fig. 4. Dye flow visualization of the LEVs evolution at three typical stroke phases. The model wing was translating from the left to the right with a fixed angle of attack of 60°. The dyes were released at the leading-edge. Lp, the primary vortex; Lm1, Lm2 and Lm3, the minor vortices. (Data taken from Lu et al., 2007.)

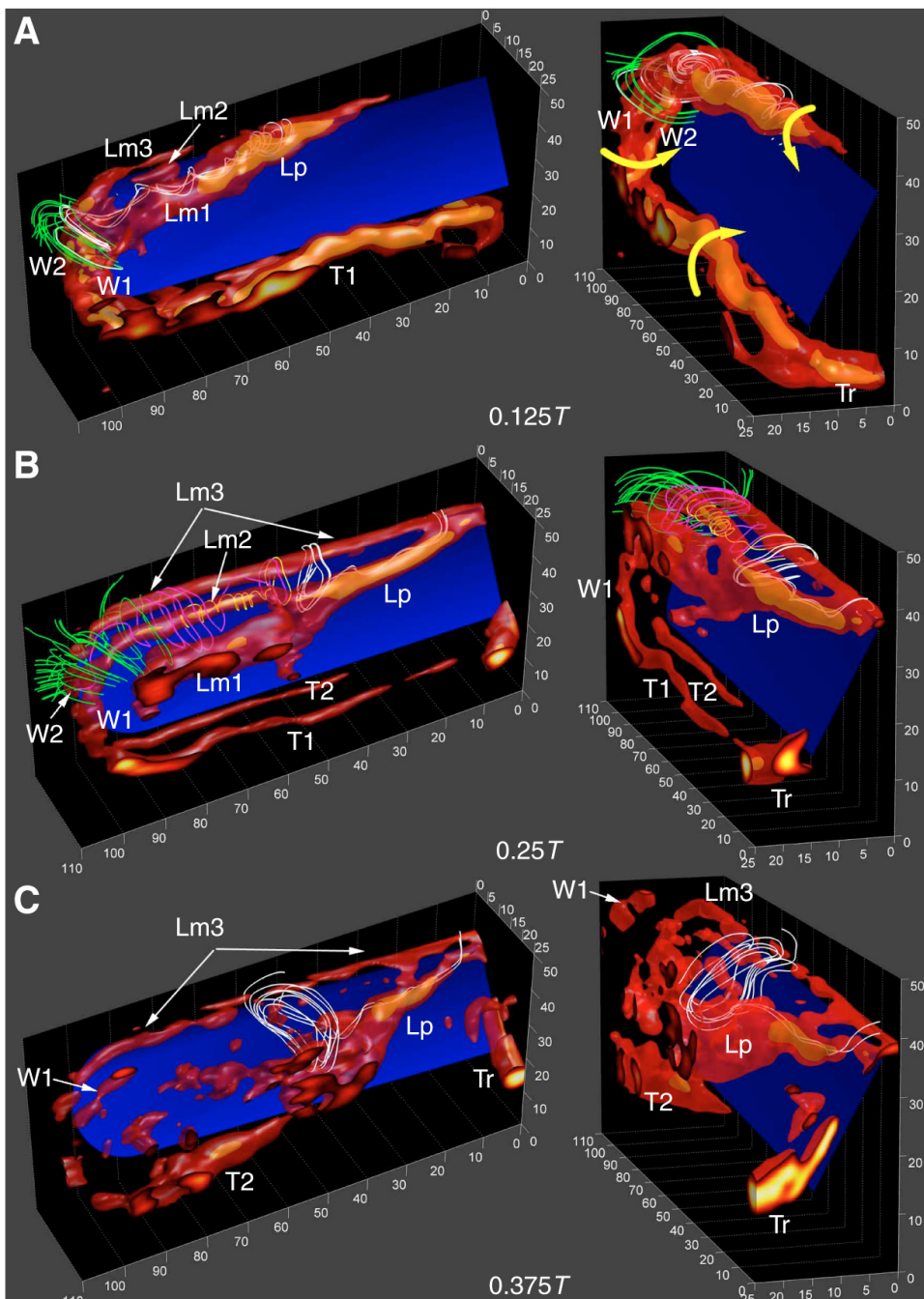


Fig. 5. DSPIV result of the 3-D flow structures and evolution of the vortices on the model wing at three typical stroke phases. The left and right image sequences are viewed from two perspectives. Isosurfaces of the Q -value are plotted to educe the vortices. The normalized values of the external red and internal yellow isosurfaces are 0.09 and 0.36, respectively. Lp, the primary vortex; Lm1, Lm2 and Lm3, the minor vortices; T1 and T2, trailing-edge vortices (TEVs); Tr, the root of TEV; W1 and W2, wing-tip vortices (WTVs). The thick yellow curved arrows denote the rotational directions of the vortices. The white instantaneous streamlines in Lp in all images are spiraling towards the wing-tip; the magenta (released at the wing-tip) and yellow (released at the outer wing within Lm2) streamlines in 0.25T are heading towards the wing-base and meet the white streamlines at the breakdown location of Lp; the green streamlines belong to the WTVs.

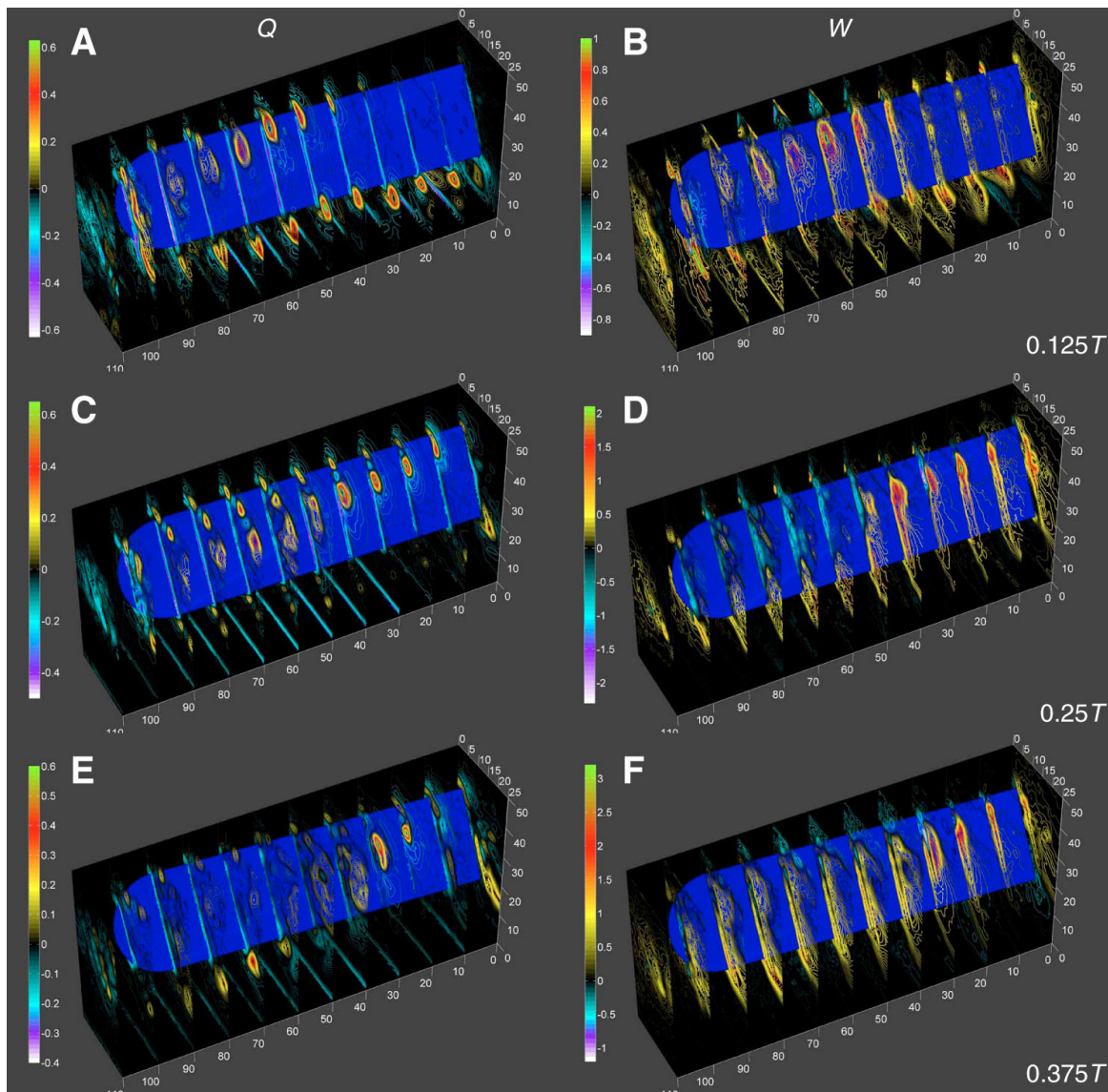


Fig. 6. The Q - and W -contours at different spanwise locations at three typical stroke phases. Positive Q -contours denote the vortex cores, while negative Q -contours denote the strain-dominating regions. The Q -values are normalized by the maximum in each stroke phase. Positive W indicates the spanwise flow heading towards the wing-tip, while negative W indicates the opposite direction. The values of W are normalized by the mean wing-tip speed.

RESULTS

The dye visualization pictures obtained from our previous study (Lu et al., 2007) are provided in Fig. 4 for comparison. In Fig. 5, the 3-D vortical structures are visualized using two levels of Q -isosurfaces. Two perspectives are provided in evolutionary sequence. The contour slices of Q and W (the spanwise velocity component) are shown in Fig. 6 to complement the detailed interior flow features.

Flow fields in the stroke phase of 0.125T

At this instant, the wing has completed pronation and is accelerating with a fixed mid-stroke angle of attack ($\alpha_{\text{mid}}=60^\circ$).

The DSPIV reconstruction in Fig. 5A shows a general hairpin-like vortical system on the wing, constituted by the LEV, the trailing-edge vortex (TEV) and the wing-tip vortex (WTV). The LEV is, in fact, a collection of four elements: one primary vortex (Lp) and three minor vortices (Lm1, Lm2 and Lm3). The TEV is denoted

T1 at this instant because another component of it will be created and shown in the next phase. The WTV, although generally seeming to be a single vortex, has shown a trend to break up into two substructures: W1 and W2. The dye visualization does not show such a hairpin because the dyes were only released at the leading edge.

Both of the DSPIV and dye pictures indicate that there is no LEV structure at the inner part of the wing (Fig. 5A and Fig. 6A). This is mainly due to the low local wing speed, which cannot cause intense flow separation and form a vortex. The DSPIV result shows that at the mid portion of the wing, the primary vortex Lp has been created and is of considerable strength attaching on the leading edge (see Fig. 6A). However, this is not shown in the dye visualization (Fig. 4A), because the region where the Lp stays is clouded by the remaining structures left in the previous stroke stages.

At the outer wing, the minor vortices Lm1 and Lm2 have been shed (see Fig. 4A, Fig. 5A, Fig. 6). Together with the outboard

minor vortex (Lm3) that remains on the leading edge, they constitute a vortex street. Thus, our previous observation of the outer wing LEV shedding (Lu et al., 2006) is confirmed. At this time, Lm1 connects well with Lp and shows no evident boundary. They were virtually both parts of a single vortex, which links to W1 via Lm1 (Fig. 5A).

Several typical instantaneous 3-D streamlines are plotted and further reveal the flow field features. The white LEV streamlines belong to the LEV and start at roughly the mid wing. They are spiraling out, stop and meet the green WTV streamlines at the wing-tip. The path traveled by the white streamlines includes Lp and Lm1, indicating that there must be substantial spanwise flows within these structures. And this is confirmed in Fig. 6B. Positive W is strong in Lp and Lm1. The maximal value appears at the mid wing and is completely comparable with the mean wing-tip speed.

Flow fields in the stroke phase of 0.25 T

At this instant, the translation of the wing reaches maximum speed. Generally speaking, the hairpin system is further diversified and becomes more complicated.

The wing acceleration enhances the streamwise (or chordwise) convection, the rate of which is greater at the outer wing due to the spanwise distribution of the wing speed. Consequently, the outer wing portion of the primary vortex Lp is at first peeled from the leading edge, and spreads to its mid and inner wing portions. Meanwhile, also due to the wing acceleration, the flows at the inner wing can be separated intensively, making the formation of the local vortex possible. By contrast, the reverse spanwise flow created by the WTVs pushes the outer wing flows towards the inner wing. The above combined process not only leads to the deviation of Lp from the leading edge, but also the migration of its origin from the mid wing to the wing-base (compare Fig. 4B with Fig. 5B). Despite these spatial changes, Lp is still bound to the wing surface.

From Fig. 5B, we see that Lp is slightly conical in structure, because at this stage Lp begins to break down at its tip. Vortex breakdown is a dramatic change at some points of a vortex, including axial speed drop and vortex core expansion (Leibovich, 1984). The 3-D streamlines are plotted to highlight this flow phenomenon: the white streamlines released near the wing-base are spiraling out, expand and stop around the breakdown location (at $0.66R$) (Fig. 5B). The dye visualization does not show violent breakdown of Lp, probably because the dyes had not reached the breakdown location at this time, or the beginning of the breakdown did not cause any violent change in the local flow field (Fig. 4B). Actually, the current breakdown location is closer to the wing base than those reported in previous studies (Van Den Berg and Ellington, 1997; Liu et al., 1998), which were at $0.75R$. In addition, strong spanwise flow indeed exists in Lp (Fig. 6D), where the peak speed was over twice the mean wing-tip speed, and twice the previously reported values (Van Den Berg and Ellington, 1997; Liu et al., 1998).

At the outer wing, Lm1 and Lm2 are convected downstream with enlarging distance between them (Fig. 5B). The dye visualization clearly demonstrated such a trend (compare Fig. 4A, B), which is also displayed by the high strain-rate regions indicated with negative Q -regions between the vortices in Fig. 6C. By contrast, WTV is completely separated into W1 and W2. Through the above dynamic process, Lm2, W1 and T1 are separated from the initial hairpin, and they form a new sub-hairpin (Fig. 5B).

Lp develops towards the wing base and is static with respect to the wing surface because of its attachment, while Lm1 is convected

downstream. These relative movements cause Lm1 to be split from Lp. This phenomenon more clearly in Fig. 5B, right column. Since it is no longer supplemented with vorticity from the wing boundary, Lm1 is diffused dramatically by the viscosity, and becomes structurally unstable (see Fig. 5B, Fig. 6C). By contrast, Lm2 is somewhat strengthened, having been stretched by the reverse spanwise flow (see Fig. 6D) and linked to the breakdown portion of Lp. At this time, the vortex street at the outer wing becomes more conspicuous (see Fig. 5B).

The deviation of Lp leaves certain space at the mid and inner sections of the leading edge, where the flow keeps on separating and creating vorticity. Consequently, Lm3 is established at the mid and inner sections of the leading edge. Eventually, all spanwise segments of Lm3 connect together along the leading edge (Fig. 5B and Fig. 6C). As a matter of fact, the inner wing sections of Lp and Lm3 refer, respectively, to the primary vortex and minor vortex of the dual-LEV, identified and confirmed in our previous studies (Lu et al., 2006; Lu et al., 2007).

Similarly, Lm3, W2 and T2 form another sub-hairpin behind that constituted by Lm2, W1 and T1 (Fig. 5B). Hence, as far as the whole vortical system is concerned, the shedding at the outer wing represents the shedding of the hairpin vortex.

Another interesting phenomenon is the watershed of spanwise flows established at the breakdown location of Lp. From Fig. 6D we see that on its inner and outer wing sides, the positive and reverse spanwise flows dominate, respectively. We plot two typical streamlines to highlight the existence of the reverse spanwise flow. In Fig. 5B, the magenta streamline starts at the wing tip and is spiraling with a loose structure towards the breakdown location. The yellow streamline in Lm2 is released at about $0.84R$ and it also stops around the breakdown location. In fact the computational study (Liu et al., 1998) reported the reverse spanwise flow within the outer wing LEV, which was denoted LEV2 in that study. However, this structure was created near the end of the downstroke (Liu et al., 1998), which is later than the result of our present study.

Flow fields in the stroke phase of 0.375 T

At this instant, the wing is decelerating. With the deceleration of the stroke, the whole vortical system on the wing is considerably dissipated.

At this time, the breakdown of Lp becomes more dramatic, as exhibited by the dye visualization (Fig. 4C) and also supported by the DSPIV result (Fig. 5C). We can see from Fig. 5C (or Fig. 6E) that both the tip of Lp and its streamlines expanded much more dramatically compared to the prior phase of 0.25 T . The breakdown region is shed from the wing, making some part of it out of the measurement window. This dramatic change of the tip results in a torch-like structure for Lp (see Fig. 5B). Moreover, the breakdown location moves into $0.57R$ and further deviates from the leading edge (see Fig. 4C, Fig. 5C and Fig. 6E).

By contrast, there is no concrete structure of Lm1, Lm2 and W2, and W1 is very distant from the wing (see Fig. 5C, right). In addition, Lm3 is considerably weakened and is collapsed into several discrete segments: the outer wing segments are shed; the inner wing segments, although not shed, are detached from the leading edge with a certain distance (Fig. 6F).

Nevertheless, the spanwise flow in Lp does not drop. Instead, its maximum is increased to over three times the mean wing-tip speed. Moreover, the watershed vanishes and the positive spanwise flow again dominates over the wing.

At this time, T2 keeps on growing at the outer wing, while T1 has completely moved out of the measurement window. The

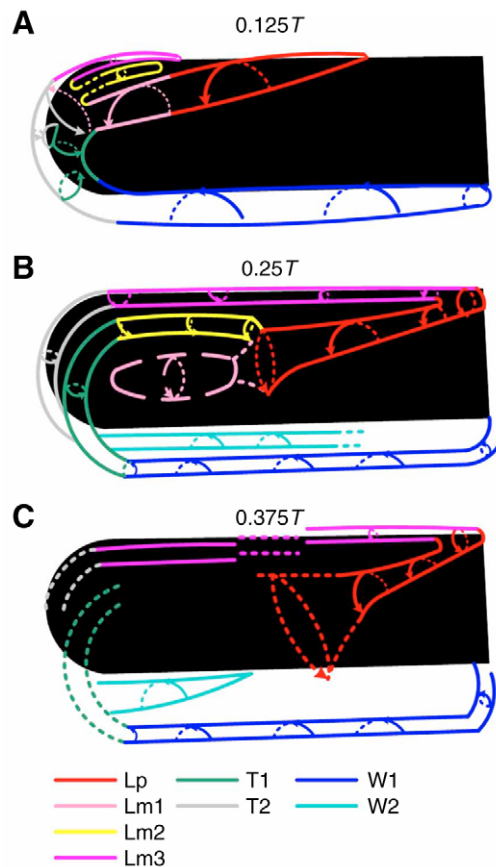


Fig. 7. Sketch of the evolution of the vortices on a flapping wing. The black region is the wing. Broken lines indicate the breakdown or collapse of the vortices.

orientation of Tr becomes parallel to the wing chord, indicating the downstream movement of $T1$.

The evolution of the vortical system is summarized schematically in Fig. 7.

DISCUSSION

The nature of the LEV system on a flapping wing

The present results reveal that in the hovering condition at high Re (~ 1000) the LEV system on a flapping wing is, in fact, a complex collection of four vortical elements: one primary vortex (Lp) and three minor vortices ($Lm1$, $Lm2$ and $Lm3$), instead of a single conical vortex, as reported previously (Ellington et al., 1996; Van Den Berg and Ellington, 1997; Liu et al., 1998; Birch et al., 2004).

We used a model dragonfly wing with high AR and without a curved leading edge. In our earlier study (Lu et al., 2006), however, DPIV measurements demonstrated that the sectional flow structure of the LEV system was not sensitive to AR and the leading-edge curvature, and the dye visualizations showed similar evolutionary process of the LEV system. We estimate that in the hovering condition at high Re , the 3-D flow structure and evolution of the flapping wing LEV system shown in the present study could, in general, be the basic pattern. Other geometric factors such as corrugation, camber and twist were not considered here; these are certainly of interest and should be studied to see how their effects alter or interact with the basic structures shown in this study.

Nevertheless, at low Re (~ 100) the LEV system would be different in structure: the spanwise flow would be weaker (Birch et al., 2004;

Lu et al., 2006) and exist behind the LEV region (Poelma et al., 2006), and the sub LEV structures would not be so dramatic (Lu et al., 2006). In fast forward flight, the structure of the LEV system could also be changed: the flows would become more attached to the wing as the increase of the flight speed (or advanced ratio) (Sun and Wu, 2003; Wang and Sun, 2005).

Here, it is necessary to clarify two terms related to the flapping wing LEV system.

(1) The 'LEV'. This term, frequently addressed in previous studies, could have different meanings at high and low Re . At high Re , the vortex labeled 'LEV', visualized and measured previously (Ellington et al., 1996; Van Den Berg and Ellington, 1997; Birch et al., 2004), should refer to Lp . Of the elements of the LEV system, Lp is strongest and most evident, making it the first element to be discovered (Ellington et al., 1996). At low Re , the sub LEV structure was not observed (Lu et al., 2006), thus the term 'LEV' could refer to the simplex vortical structure attached on the leading edge (Dickinson et al., 1999; Birch and Dickinson, 2001; Birch et al., 2004).

(2) The 'dual-LEV'. Now we know that this vortical structure, which was identified (Lu et al., 2007) and confirmed (Lu et al., 2006) in our previous studies, is constituted by the mid and inner sections of Lp and $Lm3$ at mid-stroke. It is virtually a subset of the LEV system at a certain stroke phase when a wing flaps at certain high α_{mid} and Re .

In our previous work (Lu et al., 2006), based on the structural similarities, we tried to gain insight from the realms of delta wings (Gordnier and Visbal, 2003; Taylor and Gursul, 2004; Henning et al., 2005) to explain the formation of the dual-LEV (Lu et al., 2006). Admittedly, such an idea has an intrinsic problem. The delta wings were fixed and the visualizations were conducted when the flows reached the steady state; the hypotheses of the dual-LEV formation were made according to the steady-state flow pictures. However, in the case of flapping wing, the flow field is highly unsteady and has no chance of reaching a steady state due to the dynamic motions of the wing. The present result demonstrates that the dual-LEV is a consequence of the dynamic evolution of the LEV system. In general, its formation is directly related to the movement of Lp as well as the vortex establishment of $Lm3$ at the inner wing.

The 'stay properties' of the LEV elements on a flapping wing

In our previous study (Lu et al., 2006), we reported our preliminary results demonstrating that at different spanwise locations the LEVs have distinct flow behaviors. From the results of the present study, it appears that these flow behaviors are specified as the stay properties, which worsen as they approach the wing tip: (1) at the inner wing, Lp is attached well on the wing; (2) at the mid wing, Lp breaks down; (3) at the outer wing, $Lm1$ and $Lm2$ are shed.

The attachment of the flapping LEV system has been well known for a long time (Ellington et al., 1996; Van Den Berg and Ellington, 1997; Liu et al., 1998; Dickinson et al., 1999; Birch and Dickinson, 2001; Birch et al., 2004). The LEV breakdown has also been confirmed (Liu et al., 1998; Birch et al., 2004; Lu et al., 2006; Lu et al., 2007). The outer wing LEV shedding has only been reported in a computational study (Luo and Sun, 2005) and in our previous paper (Lu et al., 2006), but is now confirmed by the results of the present study. The existence of the shedding of the outer wing minor vortices could impact the spanwise pressure distribution (Luo and Sun, 2005). Nevertheless, the resultant vortex dynamics should essentially be unchanged since large part of the force is produced by the attached primary vortex.

With the current images, we also show that the stay property of the whole LEV system is worsened as the stroke proceeds. During the wing acceleration, L_p begins to break down, and $Lm1$ and $Lm2$ become more distant from the wing. During the wing deceleration, the breakdown of L_p is intensified, and $Lm1$ and $Lm2$ are dramatically dissipated. Therefore, the direct acting area of the LEV system upon the wing is reduced with time during a stroke. Nevertheless, the vortex dynamics may not necessarily be decreased with the same manner (Wu and Sun, 2004), since the primary vortex is the dominating element responsible for the vortex dynamics on the flapping wing and during the wing acceleration it is being strengthening.

The spanwise flows

The spanwise flow in the LEV region is a hot topic in the field of flapping wing as it is considered to be one of the crucial factors responsible for the stability of the LEV at high Re (Ellington et al., 1996; Van Den Berg and Ellington, 1997; Liu et al., 1998; Birch et al., 2004). The results of the present study indicate that the spanwise flows are time-dependent, not only in the magnitude of the velocity but also in the direction.

At the early stage of the stroke, spanwise flow exists mainly at the mid and outer sections of the wing (Fig. 6B), in agreement with our earlier dye visualization studies (Lu et al., 2007) and supporting the computational results (Liu et al., 1998). As the wing accelerates, this positive spanwise flow moves into the inner section of the wing, accompanying the emergence and growth of the reverse spanwise flow at the outer wing. The competition of these two opposite spanwise flows eventually causes the breakdown of the primary vortex and establishes a watershed at the breakdown location (see Fig. 6D). Liu et al. also reported a similar phenomenon of diversification of the spanwise flows, but it appeared at a later phase than our result (Lu et al., 1998). In the real dragonfly free flight (Thomas et al., 2004), the non-uniformity of the spanwise flow direction was also visualized, and was reported to depend on the degree of sideslip. This implies that the incoming flow introduced in the experiment might play a role in causing the change of the direction of the spanwise flows. During the wing deceleration, the positive spanwise flow not only regains control over the whole wing but is even also strengthened, regardless of the collapse of the primary vortex (Fig. 6F). This phenomenon has seldom been reported.

At high Re , a strong positive spanwise flow is always found in the LEV region (actually in L_p), which is able to 'drain' the vorticity and prevent the overexpansion (instability) of the LEV (L_p) (Ellington et al., 1996; Van Den Berg and Ellington, 1997; Birch et al., 2004). According to the present result, however, the effect of this vorticity transportation to the stabilities of the LEV elements is limited. From a certain phase of the stroke, the appearance of the reverse spanwise flow begins to block further transportation of the L_p vorticity into the wake. Therefore, the vorticity is accumulated at the tip of L_p , causing local instability and eventually the breakdown. At the outer wing, though holding (reverse) spanwise flow, $Lm1$ and $Lm2$ are still unable to avoid being shed. Compared with the hawkmoth studies (Ellington et al., 1996; Van Den Berg and Ellington, 1997; Liu et al., 1998), the current maximal speed of the spanwise flow in the primary vortex is higher, over twice their reported values. Our preliminary estimate is that that AR might be a factor. Some studies on free flight of real insects argued that spanwise flows were not dominant (Thomas et al., 2004; Bomphrey et al., 2005). It is difficult to rule out the effect of incoming flow to the LEV system and the spanwise flows, however, because it is one major difference between their studies and the hovering

experiments (Ellington et al., 1996; Van Den Berg and Ellington, 1997; Liu et al., 1998; Birch et al., 2004; Lu et al., 2006; Lu et al., 2007).

At low Re values (~ 100), the spanwise flow was detected behind the LEV region (Poelma et al., 2006), and the stability mechanism of the LEV structure could be different (Wang, 2000b; Birch and Dickinson, 2001; Poelma et al., 2006).

The LEV systems on flapping wings and sweepback fixed wings

It was found that when Re reaches the order of 1000, the leading-edge flow structures on the flapping wings are analogous to those on the fixed delta wings, for example, the conical primary vortex, the intense spanwise flow, the LEV breakdown and the dual-LEV structure (Ellington et al., 1996; Van Den Berg and Ellington, 1997; Liu et al., 1998; Birch et al., 2004; Lu et al., 2006; Lu et al., 2007).

Undoubtedly, the leading edges are the vorticity-feeding sources for the LEV systems of both kinds of wings. However, the other flow mechanisms are totally distinct. The delta wings are static; the sweepback of the wing is the most significant factor responsible for the flow field behaviors, as it allows the incoming flow to have a velocity component along the leading edge, which transports the leading-edge vorticity outward and thus stabilizes the primary vortex of the LEV system (Wu et al., 1991). Unlike the delta wing, flapping wings are highly dynamic; the revolving nature of the flapping motion creates the linear spanwise distribution of the wing speed, which induces the spanwise pressure gradient, centrifugal acceleration and the Coriolis acceleration (Van Den Berg and Ellington, 1997). Either one of these effects or their combination could be the impetus for the generation of the positive spanwise flow (Van Den Berg and Ellington, 1997). Also, the dynamic motions of the flapping wings lead to the time-dependent behaviors of the spanwise flows.

Furthermore, the relation between the strength of the wing-tip effect and AR is different for flapping wings and fixed wings. According to the classical fixed wing theory, it is well known that the higher the AR of a wing, the weaker the wing-tip effect, and the better is the lift performance. As to a flapping wing, increasing the AR is bound to enhance the relative wing-tip speed, and this actually reinforces the wing-tip effect. In this case, the vorticity transportation of L_p would be blocked more severely. Hence the increase of the AR is virtually detrimental to the stability of L_p and, further, the aerodynamic performance. Nevertheless, in the realm of low Re (~ 100), where the spanwise flow is not striking while attached LEV structure is prominent (Birch and Dickinson, 2001; Birch et al., 2004; Lu et al., 2006), the wing-tip effect would play different role. Actually, it has been found that the wing-tip effect could enhance the leading-edge stability by reducing the effective angle of attack with the induced downwash (Birch and Dickinson, 2001).

Concluding remarks

In this experimental study, we implemented DSPIV and for the first time uncovered the detailed 3-D flow structure and evolution of the LEV system on a flapping wing. It is found that the LEV system is a complex collection of four vortical elements: one major vortex (L_p) and three minor vortices ($Lm1$, $Lm2$ and $Lm3$). The complexity of the LEV system is also the result of the diversifications of the spanwise flows and the stay properties of the LEV elements at different spanwise sections of the wing and at different stages of the stroke. It is of interest to see how these LEV elements behave with the forewing-hindwing interactions in the future.

LIST OF ABBREVIATIONS AND SYMBOLS

∇	gradient operator
$\nabla \mathbf{u}$	velocity gradient tensor
AR	aspect ratio (R/c)
c	mean wing chord length
d.f.	degrees of freedom
DSPIV	digital stereoscopic particle image velocimetry
f	focal length
LEV	leading-edge vortex
$Lm1, Lm2,$ $Lm3$	minor vortex
Lp	primary vortex
n	stroke frequency
o	origin
oy	translational axis
oz	rotational axis
P	pressure
Q	the 2nd invariant of $\nabla \mathbf{u}$
r	effective model wing length
R	model wing length
Re	Reynolds number
S	rate-of-strain tensor $[0.5(\nabla \mathbf{u} + \nabla \mathbf{u}^T)]$
t	time
T	stroke period
TEV	trailing-edge vortex
\mathbf{u}	velocity vector ($[U, V, W]^T$, T denotes the transpose)
U_{tip}	mean wing-tip speed
WTV	wing-tip vortex
x, y, z	coordinates in the wing-fixed frame
X, Y, Z	coordinates in the inertial frame relative to the ground (Y in the vertical direction)
α_{mid}	mid-stroke angle of attack
$\alpha(t)$	instantaneous angle of attack
Δ	discriminant of $\nabla \mathbf{u}$'s characteristic equation
ΔT_r	duration of rotation
λ_2	intermediate eigenvalue of the tensor $\Omega^2 + S^2$
ν	kinematic viscosity
ρ	fluid density
ρ_M	maximal rotational angle
$\rho(t)$	instantaneous rotational angle
$\varphi(t)$	instantaneous translational angle
Φ	stroke amplitude
ω	vorticity vector ($\nabla \times \mathbf{u}$)
Ω	rate-of-rotation tensor $[0.5(\nabla \mathbf{u} - \nabla \mathbf{u}^T)]$

We would like to take this opportunity to thank Guang Kun Tan and Guo Jun Lai for their contributions to the DSPIV developments, Ke Yu and Yu Qiao Ren for their fundamental works on the kinematics-simulation platform. This work is supported by National Natural Science Foundation 10472011 and Foundation 985-1-7 from BUAA.

REFERENCES

- Arroyo, M. P. and Greated, C. A. (1991). Stereoscopic particle image velocimetry. *Meas. Sci. Technol.* **2**, 1181-1186.
- Birch, J. M. and Dickinson, M. H. (2001). Spanwise flow and the attachment of the leading-edge vortex on insect wings. *Nature* **412**, 729-733.
- Birch, J. M., Dickson, W. B. and Dickinson, M. H. (2004). Force production and flow structure of the leading edge vortex on flapping wings at high and low Reynolds numbers. *J. Exp. Biol.* **207**, 1063-1072.
- Bomphrey, R. J., Lawson, N. J., Harding, N. J., Taylor, G. K. and Thomas, A. L. R. (2005). The aerodynamics of *Manduca sexta*: digital particle image velocimetry analysis of the leading-edge vortex. *J. Exp. Biol.* **208**, 1079-1094.
- Chakraborty, P., Balachandar, S. and Adrian, R. J. (2005). On the relationships between local vortex identification schemes. *J. Fluid Mech.* **535**, 189-214.
- Chong, M. S., Perry, A. E. and Cantwell, B. J. (1990). A general classification of three-dimensional flow fields. *Phys. Fluids A* **2**, 765-777.
- Coudert, S. J. M. and Schon, J.-P. (2001). Back-projection algorithm with misalignment corrections for 2D3C stereoscopic PIV. *Meas. Sci. Technol.* **12**, 1371-1381.
- Coudert, S., Westerweel, J. and Fournel, T. (2000). Comparison between asymmetric and symmetric stereoscopic DPIV system. In *Proceedings of the 10th International Symposium on Applications of Laser Technology to Fluid Mechanics*, pp. 6.1. Lisbon, Portugal.
- Cucitore, R., Quadrio, M. and Baron, A. (1999). On the effectiveness and limitations of local criteria for the identification of a vortex. *Eur. J. Mech. B/Fluids* **18**, 261-282.
- Dickinson, M. H., Lehmann, F.-O. and Sane, S. P. (1999). Wing rotation and the aerodynamic basis of insect flight. *Science* **284**, 1954-1960.
- Dudley, R. (2000). *Biomechanics of Insect Flight*. Princeton: Princeton Press.
- Ellington, C. P. (1984). The aerodynamics of hovering insect flight. III. Kinematics. *Philos. Trans. R. Soc. Lond. B Biol. Sci.* **305**, 41-78.
- Ellington, C. P., Van Den Berg, C., Willmott, A. P. and Thomas, A. L. R. (1996). Leading-edge vortices in insect flight. *Nature* **384**, 626-630.
- Fore, L. B., Tung, A. T., Buchanan, J. R. and Welch, J. W. (2005). Nonlinear temporal filtering of time-resolved digital particle image velocimetry data. *Exp. Fluids* **39**, 22-31.
- Gordnier, R. E. and Visbal, M. R. (2003). Higher-order compact difference scheme applied to the simulation of a low sweep delta wing flow. AIAA Paper, 2003-0620, www.aiaa.org.
- Hama, F. R. (1962). Streaklines in a perturbed shear flow. *Phys. Fluids* **5**, 644-650.
- Henning, A., Rutten, M., Wagner, C. and Raffel, M. (2005). A stereo PIV investigation of a vortex breakdown above a delta wing by analysis of the vorticity field. AIAA Paper, 2005-4908, www.aiaa.org.
- Hunt, J. C. R., Wray, A. A. and Moin, P. (1988). Eddies, stream, and convergence zones in turbulent flows. In *Center for Turbulence Research Report*, pp. 193-208. Stanford, USA: Center for Turbulence Research.
- Jeong, J. and Hussain, F. (1995). On the identification of a vortex. *J. Fluid Mech.* **285**, 69-94.
- Lawson, N. J. and Wu, J. (1997a). Three-dimensional particle image velocimetry: experimental error analysis of a digital angular stereoscopic system. *Meas. Sci. Technol.* **8**, 1455-1464.
- Lawson, N. J. and Wu, J. (1997b). Three-dimensional particle image velocimetry: error analysis of stereoscopic techniques. *Meas. Sci. Technol.* **8**, 894-900.
- Leibovich, S. (1984). Vortex stability: survey and extension. *AIAA J.* **22**, 1192-1206.
- Liu, H., Ellington, C. P., Kawachi, K., van den Berg, C. and Willmott, A. P. (1998). A computational fluid dynamic study of hawk moth hovering. *J. Exp. Biol.* **201**, 461-477.
- Lu, Y., Shen, G. X. and Lai, G. J. (2006). Dual leading-edge vortices on flapping wings. *J. Exp. Biol.* **209**, 5005-5016.
- Lu, Y., Shen, G. X. and Su, W. H. (2007). Flow visualization of dragonfly hovering via an electromechanical model. *AIAA J.* **45**, 615-623.
- Luo, G. Y. and Sun, M. (2005). The effects of corrugation and wing planform on the aerodynamic force production of sweeping model insect wings. *Acta Mech. Sinica* **21**, 531-541.
- Norberg, R. A. (1975). Hovering flight of the dragonfly *Aeschna Juncea* L., kinematics and aerodynamics. In *Swimming and Flying in Nature* (ed. T. Y. Wu, C. J. Brokaw and C. Brennen), pp. 763-781. New York: Plenum Press.
- Poelma, C., Dickson, W. B. and Dickinson, M. H. (2006). Time-resolved reconstruction of the full velocity field around a dynamically-scaled flapping wing. *Exp. Fluids* **41**, 213-225.
- Prasad, A. K. and Jensen, K. (1995). Scheimpflug stereocamera for particle image velocimetry in liquid flows. *Appl. Optics* **34**, 7092-7099.
- Saffman, P. G. (1992). *Vortex Dynamics*. New York: Cambridge University Press.
- Shavit, U., Lowe, R. J. and Steinbuck, J. V. (2006). Intensity capping: a simple method to improve cross-correlation PIV results. *Exp. Fluids* **42**, 225-240.
- Soloff, S. M., Adrian, R. J. and Liu, Z. C. (1997). Distortion compensation for generalized stereoscopic particle image velocimetry. *Meas. Sci. Technol.* **8**, 1441-1454.
- Srygley, R. B. and Thomas, A. L. R. (2002). Unconventional lift-generating mechanisms in free-flying butterflies. *Nature* **420**, 660-664.
- Sun, M. and Tang, J. (2002). Unsteady aerodynamic force generation by a model fruit fly wing in flapping motion. *J. Exp. Biol.* **205**, 55-70.
- Sun, M. and Wu, J. H. (2003). Aerodynamic force generation and power requirements in forward flight in a fruit fly with modeled wing motion. *J. Exp. Biol.* **206**, 3065-3083.
- Sveen, J. K. (2004). *An Introduction to MatPIV v.1.6.1*. Cambridge: Center for Mathematical Sciences, Department of Applied Mathematics and Theoretical Physics, University of Cambridge.
- Taylor, G. S. and Gursul, I. (2004). Buffeting flows over a low-sweep delta wing. *AIAA J.* **42**, 1737-1745.
- Thomas, A. L. R., Taylor, G. K., Srygley, R. B., Nudds, R. L. and Bomphrey, R. J. (2004). Dragonfly flight: free-flight and tethered flow visualizations reveal a diverse array of unsteady lift-generating mechanisms, controlled primarily via angle of attack. *J. Exp. Biol.* **207**, 4299-4323.
- Van Den Berg, C. and Ellington, C. P. (1997). The three-dimensional leading-edge vortex of a 'hovering' model hawkmoth. *Philos. Trans. R. Soc. Lond. B Biol. Sci.* **352**, 329-340.
- Wang, J. K. and Sun, M. (2005). A computational study of the aerodynamics and forewing-hindwing interaction of a model dragonfly in forward flight. *J. Exp. Biol.* **208**, 3785-3804.
- Wang, Z. J. (2000a). Two dimensional mechanism for insect hovering. *Phys. Rev. Lett.* **85**, 2216-2219.
- Wang, Z. J. (2000b). Vortex shedding and frequency selection in flapping flight. *J. Fluid Mech.* **410**, 323-341.
- Wang, Z. J. (2004). The role of drag in insect hovering. *J. Exp. Biol.* **207**, 4147-4155.
- Willert, C. (1997). Stereoscopic digital particle image velocimetry for application in wind tunnel flows. *Meas. Sci. Technol.* **8**, 1465-1479.
- Wu, J. H. and Sun, M. (2004). Unsteady aerodynamic forces of a flapping wing. *J. Exp. Biol.* **207**, 1137-1150.
- Wu, J. Z., Vakil, A. D. and Wu, J. M. (1991). Review of the physics of enhancing vortex lift by unsteady excitation. *Prog. Aerosp. Sci.* **28**, 73-131.